Deposition of Droplets onto Solid Objects in Aerosol Flow

by

Bojan Petkovic
B.Sc., University of Novi Sad, Serbia, 2004

A THESIS SUBMITTED IN PARTIAL FULFILLMENT OF THE
REQUIREMENTS FOR THE DEGREE OF
MASTER OF APPLIED SCIENCE

in

THE FACULTY OF GRADUATE STUDIES
(Chemical and Biological Engineering)

THE UNIVERSITY OF BRITISH COLUMBIA
(Vancouver)

February 2010

Abstract

In this work, the effect of velocity on deposition coefficients and capture efficiencies on a circular disk, placed normal to an aerosol flow was investigated. The superficial gas velocity was varied in the range of 0.1 m/s to 1.5 m/s, while the volume median diameter of the droplet size distribution varied between 3.9 and 7.5 microns. The morphology and distribution of deposits on the upstream and downstream surface of the disk were observed and measured. The effect of contact angles (20°, 51°, 94°) on deposition, and dry vs. wet surface effects were also investigated.

It was found that in the range of velocity and droplet sizes investigated, deposition on the upstream side was dominated by the inertial impaction mechanism. Capture efficiencies increased with velocity and droplet size, and could be explained by the inertial impaction mechanism from the upward flow, using the potential flow approximation. For the downstream side, capture efficiencies increased with droplet size and showed a minimum with velocity. It is postulated that the governing deposition mechanism for the downstream side is the inertial impaction mechanism with gravity in the flow direction.

On the upstream side, it was found that deposits were concentrated closer to the coupon edge, while on the downstream side, the distribution of deposits on the surface was uniform.

In the range of investigated contact angles, there was no significant difference observed between the deposition rates. The same can be said for the effect of dry vs. wet coupon surface.

Table of Contents

List of Tables

List of Figures

Nomenclature

A	Upstream or downstream coupon (disk) surface area, $A = D_c^2 \pi / 4$, m^2
A_{column}	Column cross section area, m^2
A_{dry}	Dry coupon (disk) surface area, upstream or downstream, m^2
A_{an}	Annular area between the rotameter float and the rotameter tube, m^2
A_{tube}	Cross section area of the rotameter tube, m^2
A_{wet}	Wet coupon (disk) surface area, upstream or downstream, m^2
Br	Blockage ratio, $Br=A/A_{column}$, *dimensionless*
c_b	Aerosol concentration in the bulk, kg/m^3
C_c	Cunningham slip correction factor, *dimensionless*
C_p	Heat capacity, $J \cdot kg^{-1}K^{-1}$
c_{wake}	Aerosol concentration in the wake, kg/m^3
d	Characteristic length (total disk surface area divided by the perimeter of a disk, $D_c/2$), m
D	Brownian diffusivity, m^2/s
D_c	Coupon (disk) diameter, m
D_{min}	Minimum drop diameter, m
D_{max}	Maximum drop diameter, m
D_p	Particle (droplet) diameter, m
$D_{p,eq}$	Equivalent diameter for a given drop size distribution that has the same specific mass, m_s, as that size distribution, m

$D_p^{'}$ Particle (droplet) diameter on a surface, having diameter D_p in the aerosol, $D_p^{'} = k(\theta) \cdot D_p$, *m*

$D_{p,i}$ Drop diameter of the class *i* in the aerosol, *m*

$D_{p,max}$ Drop diameter of the last (maximum) class in the aerosol, *m*

$D_{p,reference}$ Reference particle (droplet) diameter, *m*

$D_{V,10}$ 10% volume diameter, *m*

$D_{V,50}$ Volume median diameter, same as *VMD*, *m*

$\overline{D}_{V,50}$ Average volume median diameter, *m*

$D_{V,90}$ 90% volume diameter, *m*

E Capture efficiency, *dimensionless*

E_a Activation energy, *J/mol*

$E_{i,downstream}$ Capture efficiency of the class *i*, for the downstream side, *m/s*

$E_{i,upstream}$ Capture efficiency of the class *i*, for the upstream side, *m/s*

F Force, *N*

$F_{a,nozzle}$ Volumetric flow rate of air to the nozzle, at pressure p_{nozzle}, m^3/s

$F_{a,secondary}$ Volumetric flow rate of secondary air to the gas distributor, at pressure $p_{secondary}$, m^3/s

F_l Droplet (liquid) flow rate to the aerosol, *kg/s*

g Gravity acceleration, g=9.81, m/s^2

i_{max} Largest diameter class in the distribution, *dimensionless*

h Height of air annulus (in the nozzle), *cm*

H_f Residence time of inertialess particles, *dimensionless*

H_p Residence time of particles with inertia, *dimensionless*

k	Correction factor for the drop size estimated by correlation, *dimensionless*
$k(\theta)$	Drop diameter correction factor, for a drop sitting on a surface, *dimensionless*
k_B	Boltzmann's constant, $k_B = 1.386 \cdot 10^{-23}$, $kg \cdot m^2 \cdot s^{-2} \cdot K^{-1}$
k_d	Particle (droplet) deposition coefficient (velocity), *m/s*
$k_{i,downstream}$	Particle (droplet) deposition coefficient of the class *i*, for the downstream side, *m/s*
$k_{i,upstream}$	Particle (droplet) deposition coefficient of the class *i*, for the upstream side, *m/s*
k_m	Mass transfer coefficient, *m/s*
k_r	First-order reaction constant, s^{-1}
$k_{r,0}$	Pre-exponential factor for the first order reaction constant, s^{-1}
k_s	Deposition constant, $k_s = r_{d,1} / (m_s A)$, s^{-1}
k_t	Particle (droplet) transport coefficient, *m/s*
k_t^+	Nondimensional particle (droplet) transport coefficient, *dimensionless*
L	Plate (surface) length, *m*
m	Mass of deposits, *kg*
M	Mass of the rotameter float, *kg*
$\dot{M}_g$	Mass flow rate of a gas (in the nozzle), *g/s*
m_i	Mass of deposits in the *i*-th layer, *kg*
$m_{i,0}$	Mass of the freshly deposited *i*-th layer, *kg*
$m_{i,f}$	Mass of the *i*-th layer at the end of reaction ($t=\infty$), *kg*

$\dot{M}_l$	Mass flow rate of a liquid (in the nozzle), *g/s*
m_s	Specific mass of a droplet sitting on a surface, kg/m^2
M_w	Molar mass of the gas, *kg/mol*
MCR	Micro Carbon Residue, *dimensionless*
N_i	Number of particles (droplets) in the class *i*, *dimensionless*
N'	Statistically corrected number of particles, *dimensionless*
p	Gravity orientation parameter {-1, 0, 1}, *dimensionless*
P	Pressure, *Pa*
P_0	Atmospheric pressure, P_0 = 101 325 *Pa*
p_i	Total detection probability, *dimensionless*
$p_{i,Border}$	Detection probability due to the border correction, *dimensionless*
$p_{i,DOF}$	Detection probability due to the depth of field correction, *dimensionless*
P_{nozzle}	Pressure of the air in the nozzle, *Pa*
$P_{secondary}$	Pressure of the secondary air in the gas distributor, *Pa*
r	Radial coordinate, *m*
R	Universal gas constant, $R = 8.314\ J \cdot K^{-1} \cdot mol^{-1}$
R_c	Coupon (disk) radius, *m*
r_d	Deposition rate, *kg/s*
$r_{d,1}$	Deposition rate on a dry surface, *kg/s*
$r_{d,2}$	Deposition rate on a wet surface, *kg/s*
$r_{d,i}^{\exp}$	Experimental integral deposition rate for experiment *i*, *kg/s*
$r_{d,i}^{\mathrm{int}}$	Calculated integral deposition rate for experiment *i*, *kg/s*

Re Reynolds number for a disk, $\mathrm{Re} = \frac{Ud\rho_a}{\mu_a}$, *dimensionless*

R_I Interception parameter, $R_I = D_p/D_c$, *dimensionless*

$\bar{r}$ Nondimensional radial coordinate, $\bar{r} = r / R_c$, *dimensionless*

$\bar{r}_0$ Initial nondimensional radial position at $\bar{t}_0$, *dimensionless*

Sc Schmidt number, $Sc = \frac{\nu_a}{D}$, *dimensionless*

Sh Sherwood number for a disk, $Sh = \frac{k_m d}{D}$, *dimensionless*

$S_{D_{V,50}}$ Standard deviation of the volume median diameter, *m*

$S_{\bar{D}_{V,50}}$ Standard deviation of the average volume median diameter, *m*

S_p Particle stopping distance, $S_p = t_p U$, *m*

St Stokes number, $St = \frac{t_p U}{D_c}$, *dimensionless*

St_{cr} Critical Stokes number, *dimensionless*

t Time, *s*

T Temperature, *K*

t_i Moment of deposition of the *i*-th layer, *s*

t_p Particle relaxation time, $t_p = \frac{\rho_p D_p^2 C_c}{18\mu_a}$, *s*

t_p^+ Nondimensional particle relaxation time, $t_p^+ = t_p \cdot \frac{\left(v^*\right)^2}{\nu_a}$, *dimensionless*

$\bar{t}$ Nondimensional time, $\bar{t} = t \cdot v_0 / R_c$, *dimensionless*

$\bar{t}'$	Nondimensional time needed for particle to reach the coupon surface plane ($\bar{x} = 0$), *dimensionless*
Q	Volumetric flow rate of air, m^3/s
U	Superficial gas velocity, *m/s*
U_{nozzle}	Superficial gas velocity in the column, from the nozzle air, *m/s*
$U_{secondary}$	Superficial gas velocity in the column, from the secondary air, *m/s*
u_r	Radial velocity component of a particle (droplet), *m/s*
u_x	Axial velocity component of a particle (droplet), *m/s*
$\vec{u}$	Particle (droplet) velocity vector, *m/s*
V	Yield of volatiles, *dimensionless*
v_0	Axial gas velocity, same as U, *m/s*
V_g	Gas velocity (in the nozzle), *m/s*
$V_{i,aerosol}$	Volume relative frequency of the class i in the aerosol, *dimensionless*
$V_{i,downstream}$	Volume relative frequency of the class i on the downstream side of the coupon, *dimensionless*
$V_{i,upstream}$	Volume relative frequency of the class i on the upstream side of the coupon, *dimensionless*
V_l	Liquid velocity (in the nozzle), *m/s*
v_r	Radial gas velocity component, *m/s*
V_t	Terminal velocity of a particle (droplet), *m/s*
v_x	Axial gas velocity component, *m/s*
v^*	Friction velocity, *m/s*
V^*	Maximum yield of volatiles, *dimensionless*

v^{∞}	Average gas free stream velocity, *m/s*
v_r^{∞}	Freestream gas velocity in radial direction, *m/s*
$\vec{v}$	Gas velocity vector, m/s
$\bar{v}_r$	Nondimensional radial gas velocity, $\bar{v}_r = v_r / v_0$, *dimensionless*
$\bar{v}_x$	Nondimensional axial gas velocity, $\bar{v}_x = v_x / v_0$, *dimensionless*
VMD	Volume median diameter, same as $D_{V,50}$, *m*
x	Axial coordinate, *m*
$\bar{x}$	Nondimensional axial coordinate, $\bar{x} = x / R_c$, *dimensionless*
$\bar{x}_0$	Initial nondimensional axial position at $\bar{t}_0$, *dimensionless*
y	Surface coverage, *dimensionless*
z_1, z_2	Solutions of the characteristic equation, $z_{1,2} = \frac{-1 \pm \sqrt{1-16St}}{4St}$, *dimensionless*

Greek symbols

γ	Surface tension, J/m^2
γ_L	Liquid surface tension, J/m^2
γ_{LV}	Liquid-vapour surface tension, J/m^2
γ_S	Solid surface tension (surface energy), J/m^2
γ_{SL}	Solid-liquid surface tension, J/m^2
γ_{SV}	Solid-vapour surface tension, J/m^2
μ_a	Dynamic viscosity of air, $Pa \cdot s$

μ_{oil}	Dynamic viscosity of oil, $Pa \cdot s$
ν_a	Kinematic viscosity of air, m^2/s
ν_l	Kinematic viscosity of liquid (in the nozzle), $10^{-6}\ m^2/s$ (cSt)
θ	Equilibrium contact angle, °
θ_{adv}	Advancing contact angle, °
θ_{rec}	Receding contact angle, °
ρ_a	Density of air, kg/m^3
ρ_f	Density of fluid flowing through the rotameter, kg/m^3
ρ_g	Density of gas (in the nozzle), g/cm^3
ρ_p	Particle (droplet) density, kg/m^3
σ_l	Liquid surface tension (in the nozzle), $10^{-3} J/m^2$ (dyn/cm)
τ_i	Duration of the experiment i, s

List of acronyms

ATB	Atmospheric Topped Bitumen
FBP	Final Boiling Point
HGO	Heavy Gas Oil
IBP	Initial Boiling Point
LGO	Light Gas Oil
MCR	Micro Carbon Residue
MEBR	Syncrude Canada Ltd. Plant 7 Bitumen product
VTB	Vacuum Topped Bitumen

TEG	Triethylene glycol

Acknowledgments

I would like to use this opportunity to thank my supervisors, Dr. Paul Watkinson, Dr. Dusko Posarac and Dr. Fariborz Taghipour, for the supervision of my work on this thesis and all their suggestions and help.

Also, I would like to thank Syncrude Canada Ltd., for financing this project and for the opportunity to work on an interesting subject.

Finally, I would like to thank my parents for their understanding and support throughout the years.

Chapter 1. Introduction

Total oil sand reserves in Northern Alberta are estimated at around 1.7 trillion barrels of bitumen; this amount is comparable to the total proven world oil reserves of conventional petroleum, where the top seventeen countries hold about 1.24 trillion barrels [1]. One tenth of the bitumen deposits are considered economically recoverable at 2006 oil prices. This portion alone makes Canada's total oil reserves second-largest in the world, next only to Saudi Arabia's.

As the price of petroleum over the last decade showed a steady rise [2], petroleum production from unconventional oil reserves (oil sands, oil shales, biomass) [3] attracted more attention. Production of synthetic crude oil from bitumen which was extracted from oil sands, became more economically viable, resulting in a great expansion in Northern Canada. Today, 46% of the petroleum in Canada is produced from oil sands, while in 1992 that share was just 17% [4, 5].

Oil sands are a mixture of bitumen, sand, clay and water [6]. Typically, they contain about 84% wt. of solids, 11–12% wt. of crude bitumen and the rest is water. The solids are about 90% quartz, with some amounts of feldspar, muscovite, chert, and clay minerals [5]. Crude bitumen is a complex mixture of organic compounds that contains polymeric asphaltenes and resins of high molecular mass, and high levels of nitrogen, oxygen, sulfur, and metals. It is a highly viscous, black and sticky substance, entirely soluble in carbon disulfide. Its main characteristic is high viscosity in its natural state ($10^1 - 10^3$ Pa·s) – to the point of pseudoplasticity; it has to be heated or diluted before it will flow [5, 7].

For deep oil-sand deposits, steam injection is used, whereas for shallow deposits, extraction of bitumen begins with the mining process. Mining the oil sands includes removing the overlying overburden, recovering the oil sands and transporting them to a bitumen extraction plant. In the extraction plant, hot water is used to wash out bitumen from the oil sands. The bitumen is then upgraded and refined to produce synthetic crude oil.

1.1. Bitumen upgrading and the Fluid Coker

The purpose of bitumen upgrading is to reduce high boiling fractions, increase the hydrogen to carbon ratio, and remove impurities. Table 1.1 illustrates the property differences between bitumen and crude oils, which suggests a need for bitumen upgrading.

Table 1.1 Bitumen, Synthetic crude, and Conventional crude oil properties [5]

	Bitumen	Synthetic crude	Conventional crude
°API	8	32	41
Sulfur, wt %	4.8	0.08	0.2
Nitrogen, wt %	0.45	0.03	0.04
Viscosity at 40°C, cSt	3000	3.0	2.9
Pour point, °C	18	–4.5	–6
Metals, mg/kg	450	<1	
Distillate yield, vol %			
IBP – C5*	0	4	3
C5 – 195°C	0	18	36
195°C – 345°C	14	47	31
345°C – 560°C	86	31	18
560°C +		0	12

*IBP=Initial Boiling Point, C5=pentane

Upgrading consists of two steps: primary and secondary. A schematic diagram of the bitumen upgrading process and its two main steps is given in Fig. 1.1.

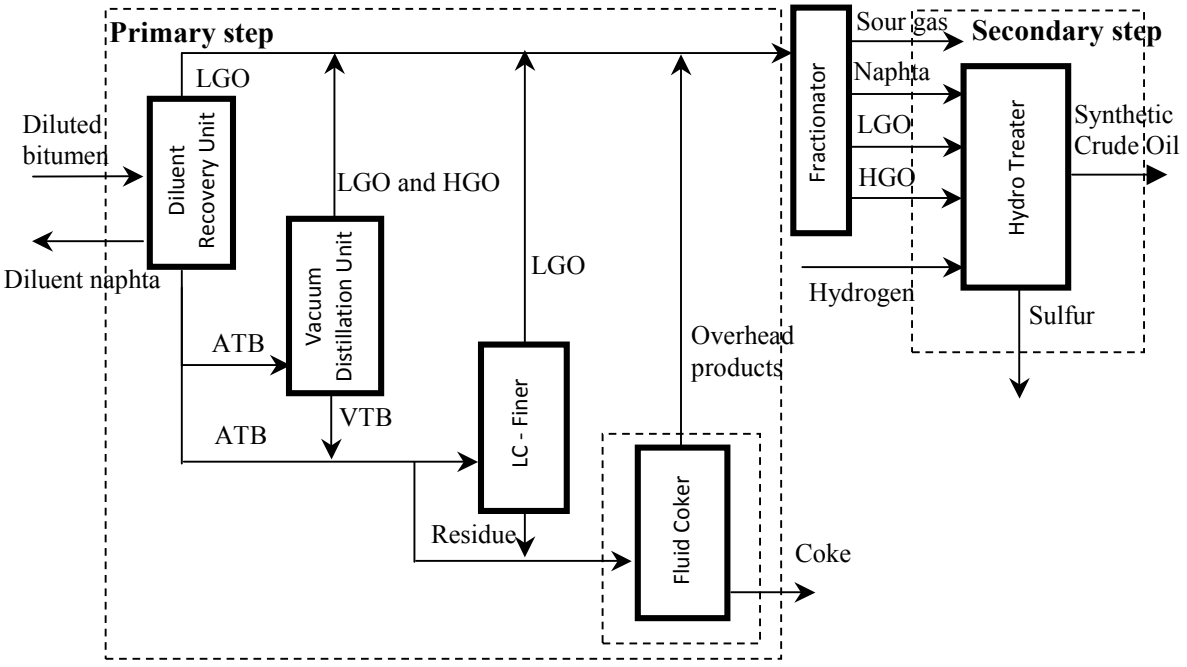

Figure 1.1 Schematic representation of the bitumen upgrading process [9]

The primary step converts high-molecular residues in the bitumen to a distillate. The *secondary step* includes separating the distillate into desired boiling ranges and adding hydrogen to saturate hydrocarbons and remove impurities.

In the primary step, bitumen from the froth treatment step is first sent to the Diluent Recovery Unit (atmospheric distillation column). This unit recovers diluent naptha, and produces Light Gas Oil (LGO) and Atmospheric Topped Bitumen residue (ATB). Produced ATB is sent to the Vacuum Distillation Unit, where LGO and Heavy Gas Oil (HGO) are removed from the top, and the Vacuum Topped Bitumen (VTB) from the bottom is mixed with part of the ATB and sent to the LC-Finer. The LC-Finer is a catalytic reactor where hydrogen is added to increase the hydrogen to carbon ratio and produce cracked LGO. Residue from the LC-Finer is combined with parts of the feed and sent to the Fluid Coker reactor (Fig. 1.2).

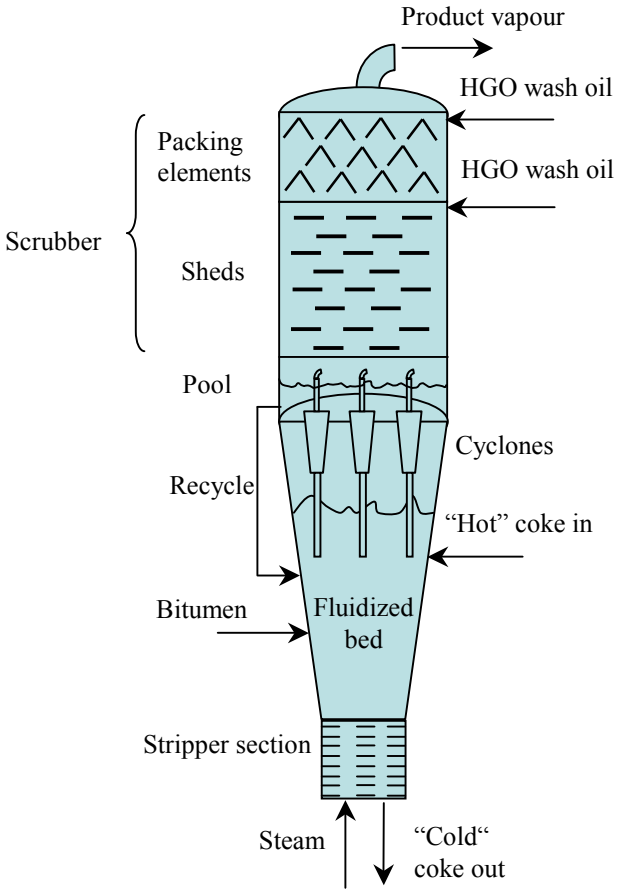

Figure 1.2 Schematic of the Syncrude Fluid Coker

In the Fluid Coker, bitumen is first sprayed into the fluidized bed reactor section. Coking reactions occur on the surface of introduced hot coke particles, at about 510°C to 530°C, where bitumen cracks and forms coke and lighter fractions in the form of vapour. Energy for the reaction is provided by burning in the coke burner part of the produced coke from the reactor, and by re-circulating the hot coke back into the reactor. In the stripping section, bitumen that remains on the surface of the coke particles is stripped off with steam. Product vapour from the coker reactor is then sent to the cyclones that remove unreacted bitumen droplets and particles above about 11 microns [7]. Vapour is then sent to the scrubber section, which consists of the pool, sheds and structured grid (Fig. 1.2). Heavy gas oil at 325°C is sprayed from the top of the structured packing and sheds, in order to cool down the gas and remove (scrub) heavy components from the vapour by condensation. The purpose of the heavy gas oil is to also remove small droplets and coke particles from the product vapour. However, if droplets and particles deposit on the surface of the packing in the Scrubber, they can cause fouling of the Scrubber and plugging of the reactor.

1.2. Fouling in the Scrubber section of the Fluid Coker

Fouling can be defined as the accumulation of unwanted material on solid surfaces. Fouling in the grid section of the scrubber in the Fluid Coker reactor increases pressure drop along the scrubber and changes the operating conditions of the reactor. The cause of fouling in the scrubber section of the reactor is deposition of fine bitumen droplets, and possibly coke particles, not removed in the cyclones from the product vapour. Under the effect of high temperatures, bitumen droplets deposited on the surface undergo thermal decomposition into volatiles and coke. Formed coke remains on the surface of the packing as a solid material. Build-up of deposits eventually results in plugging of the reactor and its shutdown for maintenance, with a costly disruption of the production. Figure 1.3 shows a comparison between the clean packing in the grid and the packing surface covered with coke.

If we could understand the fundamental phenomena that govern deposition on the packing elements of the scrubber, it would be possible to change operating conditions in

order to minimize the fouling, or change the geometry of the packing and prolong the reactor operation.

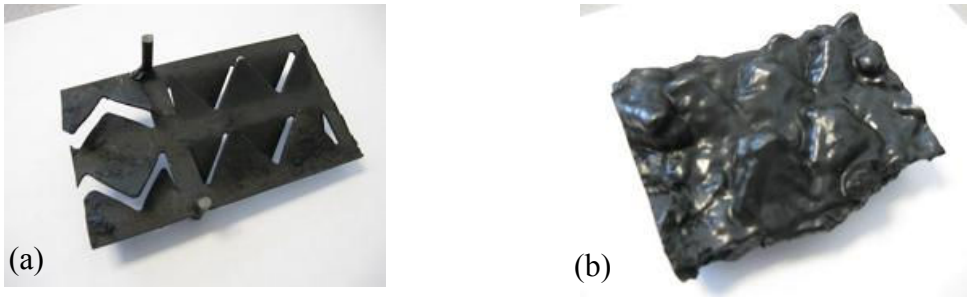

Figure 1.3 Segment of the packing elements in the Scrubber Section of the Fluid Coker, (a) before start up of the reactor and (b) after reactor shutdown

1.3. Project objectives

Fouling in the scrubber section of the Fluid Coker reactor was previously studied theoretically by Subudhi [8]. He simulated the increase in the pressure drop of the scrubber by modeling particle transport to the surface, assuming perfect sticking, and included the effect of the reaction. His model assumed flow *parallel* to the surface of the packing. Since the orientation of packing elements in the reactor is not fully parallel with the upward flow of the gas (Fig. 1.4), the fluid dynamics around such a geometry is certainly different. Since fluid dynamics plays a key role in particle transport to the surface, there was room for improvements to Subudhi's approach.

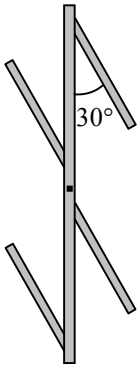

Figure 1.4 Side view of the scrubber packing elements, given in Fig. 1.3. The blades are inclined at a 30° angle with the vertical axis [8]

Because of the complex geometry of the actual packing, it was decided to study deposition onto single elements of simple geometries, placed normal to the flow of aerosol droplets in a gas-vapour mixture. A normal orientation of the disk to the flow, compared to the parallel orientation, yields a different flow field around the disk that is likely more similar to the flow field around the packing elements in the Scrubber. This is especially true for the vortex behind the disk, where flow separation occurs. The idea was to investigate deposition on the 5 cm diameter circular disk (coupon), placed in a 7.5 cm diameter column (Fig. 1.5). The aerosol flow was directed in the upward direction, as is the case in the Fluid Coker reactor.

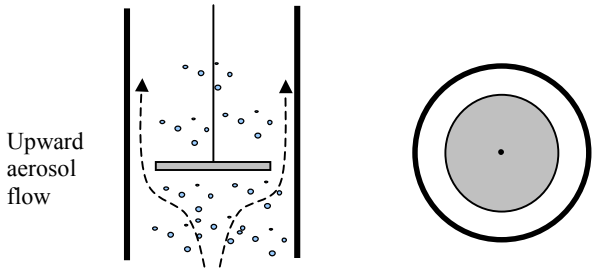

Figure 1.5 Schematic representation of the side and top view of the 5 cm diameter disk in the 7.5 cm diameter column (aerosol droplets are presented disproportionately large)

The deposition process was intended to be studied experimentally in two separate experimental units: a room temperature unit (called the Cold Unit) and a high temperature unit (called the Hot Unit). The Cold Unit was intended to be used to investigate the effect of velocity over the range that could not be covered in the Hot Unit (0–1.5 m/s), and the effect of other factors such as droplet size, which was not measured in the Hot Unit. The high temperature unit was used to study deposition of heavy oil hydrocarbons at temperatures of 290–425°C, similar to the conditions in the real Fluid Coker reactor, and the effect of heavy oil composition (Song [52]). Experimental results from both units were used for verification of the computational fluid dynamics (CFD) model predictions, undertaken as part of this overall study (Lakghomi [36]), and that would be later used for simulation of deposition on arbitrary geometries.

1.4. Scope of the thesis

The objective of this thesis was to carry out an experimental investigation of the deposition process at room temperature. For this purpose, the Cold Unit apparatus (Fig. 4.1) was constructed as part of this work. A limited set of experimental factors was selected. To investigate the effect of particle transport on deposition, velocity and droplet size distribution were varied (Sections 5.1–5.3); to quantify the distribution of deposits on the surface, distribution of deposits along the coupon radius was measured (Section 5.6). Lastly, to understand the effect of wettability on sticking and deposition, the effect of contact angles between the liquid and the solid surface was studied (Section 5.7). In particular, the factors to be investigated included:

1. Effect of superficial gas velocity on deposition rate, at a given droplet size distribution, over the range 0–1.5 m/s.

2. Effect of droplet size distribution on deposition rate, at a given velocity, over the range of volume median diameters between 3.9 and 7.5 microns.

3. Morphology of deposits and distribution of deposits along the radius of the disk.

4. Effect of contact angles (20°, 51°, and 94°) between the liquid and the solid surface on deposition rate.

In addition to the experimental investigation, the inviscid flow approximation was used to simulate particle transport to the surface and interpret the obtained experimental results (Section 5.4). Furthermore, deposition coefficients from the room temperature unit experiments (Section 5.3) were recalculated to the high temperature conditions, and compared with the independent set of data obtained in the high temperature unit experiments [52] (Chapter 6). The following chapter (Chapter 2) presents the relevant theory of particle deposition from parallel flow and flow around bluff bodies (transport and sticking) used in the modeling section (Chapter 3), and reviews significant work in this area.

Chapter 2. Theory and Literature Review

The deposition of small particles and droplets onto solid surfaces from gaseous streams was studied in the literature for two main classes of problems. First is the case when the flow is parallel to solid surfaces (laminar and turbulent flow) and the second is when the flow is normal to solid surfaces. The rationale for this division is that the flow field, and therefore the mechanisms that govern particle deposition, are different in each case. The main aspects of both are reviewed here, since both apply to the object of investigation.

2.1. Particle deposition from turbulent flow parallel to solid surfaces

Experimental work on particle deposition was reviewed by Cleaver and Yates [11], who validated their sublayer model for deposition from turbulent flow against the available experimental data. Papavergos and Hadley [10] were first to give a comprehensive review of theoretical developments and available experimental data on deposition from parallel turbulent flow. Epstein [12] presented a review of theory of particle transport, particle attachment and particle re-entrainment. Recently, deposition from parallel flows was also studied by the means of computational fluid dynamics. Tian and Ahmadi [14] compared different turbulent model predictions with the existing body of experimental data, while Zhang and Li [13] simulated deposition on the walls, roof and floor of horizontal ducts, thus distinguishing the effect of gravity.

Following Epstein [12], the main deposition phenomena can be summarized as follows. Starting from submicron particles, three mechanisms of deposition dominate as the particle size increases: diffusion, inertia and impaction. In the *diffusion regime*, particles are sufficiently small that they are carried to the wall through the viscous sublayer by Brownian diffusion. The Brownian diffusivity for a dilute suspension of spheres is given by the Stokes-Einstein equation,

$$D = \frac{k_B T}{3\pi\mu_a D_p} \tag{2.1}$$

where k_B is the Boltzmann constant, μ_a is the air dynamic viscosity and D_p is the particle diameter. It can be used in empirical correlations for convective mass transfer of the form $Sh = f(Re, Sc)$. The calculated Sherwood number yields a mass transfer coefficient, k_m, equal to the particle transport coefficient, k_t, for this case.

In the *inertia regime*, the particles are large enough so that turbulent eddies transfer to them some momentum that is normal to the walls. This momentum is not completely dissipated in the viscous sublayer and particles can reach the surface. A large body of experimental results on deposition in the inertial regime can be summarized by the following empirical correlation, to a good degree of accuracy,

$$k_t^+ = 3.5 \cdot 10^{-4} t_p^+, \quad 0.2 < t_p^+ < 20, \quad \textit{horizontal wall} \tag{2.2}$$

where k_t^+ is the nondimensional deposition coefficient. The key independent variable for the inertia regime is the nondimensional particle relaxation time, t_p^+, defined as $t_p^+ = t_p \cdot \frac{(v^*)^2}{(\mu_a / \rho_a)}$. The dimensional particle relaxation time, t_p, represents the time needed for a particle to adjust or relax its velocity to a new fluid velocity,

$$t_p = \frac{\rho_p D_p^2 C_c}{18 \mu_a} \tag{2.3}$$

where D_p is the particle diameter. It includes fluid viscosity and the Cunningham slip correction factor, C_c, and is therefore affected by changes in temperature and pressure. The deposition coefficient, k_t, can be obtained from the nondimensional deposition coefficient, k_t^+, using the relation $k_t^+ = k_t / v^*$. The friction velocity v^*, can be calculated from the shear stress or velocity gradient at the wall according to,

$$v^* = \left(\frac{\mu_a}{\rho_a} \cdot \left. \frac{dv}{dx} \right|_{x=0} \right)^{1/2} \tag{2.4}$$

The average velocity gradient, along a surface of length L, may be estimated from the correlations given in the literature (Schlichting [15], Lai and Nazaroff [16]),

$$\left.\frac{dv}{dx}\right|_{x=0} = \left(\frac{0.074}{\mu_a}\right)\left(\frac{\rho_a\left(v^{\infty}\right)^2}{2}\right)\left(\frac{v^{\infty}L}{\mu_a/\rho_a}\right)^{-1/5} \tag{2.5}$$

where v^{∞} is the average free stream velocity. To account for the effect of gravity, Sehmel [17] extended this theory to predict deposition velocities on the floor and ceiling of horizontal ducts, and obtained,

$$k_t^{+} = \begin{cases} 2\cdot 10^{-3} t_p^{+}, & 0.2 < t_p^{+} \quad Floor \\ 4\cdot 10^{-5} t_p^{+}, & 1 < t_p^{+} < 50, \quad Ceiling \end{cases} \tag{2.6a,b}$$

However, these equations fit only a limited set of data (Papavergos and Hadley [10]).

As particle size is increased, the inertia regime is followed by the *impaction regime*, which begins at $t_p^{+} = 20$, where the response of such large particles to turbulent fluctuations becomes limited, and k_t^{+} levels off at about 0.12–0.18. At $t_p^{+} \geq 30$, deposition coefficients starts to fall gradually, since such large particles get even more sluggish in their response to turbulent eddies.

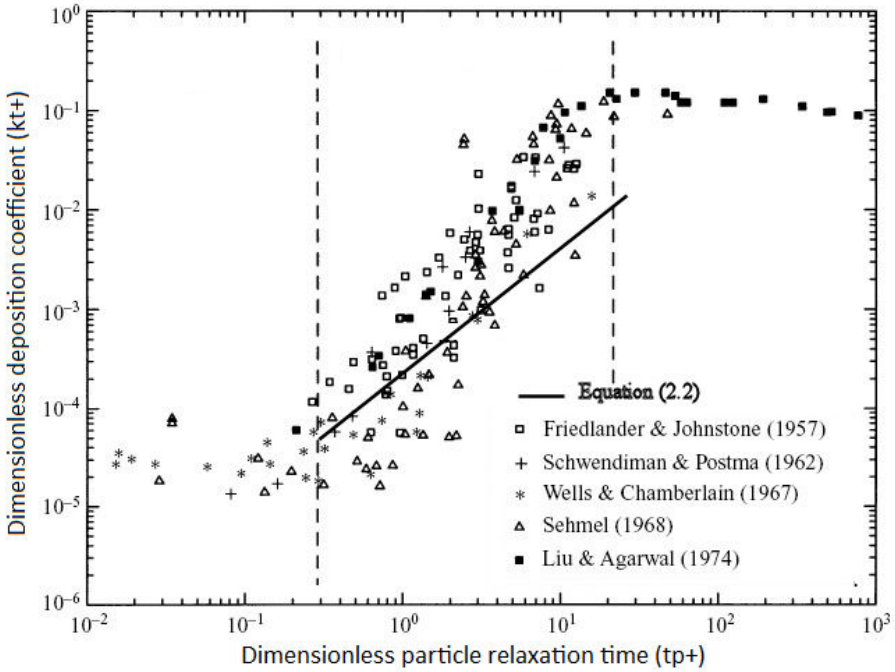

Figure 2.1 Summary of experimental data on particle deposition from turbulent pipe flow, adapted from Young and Leeming [18]

Gravitational settling becomes important for larger particles with $t_p^+ \geq 1$. The deposition coefficient, k_t, from gravitational settling then becomes equal to the particle terminal velocity, V_t. A summary of experimental data on particle deposition from turbulent pipe flow is given in Fig. 2.1 (from Young and Leeming [18]).

The above considerations are related to the transport of particles to the surface. If perfect sticking is assumed, the particle transport flux becomes equal to the particle deposition rate and vice versa. Particles can also be re-entrained into the gas stream (Epstein [12]). This phenomenon can happen with solid particles (Vincent and Humphries [19]), but in the case of organic liquid droplets deposited on hydrophilic surfaces, with low contact angles, it is reasonable to assume that re-entrainment does not occur.

2.2. Particle deposition from the flow around bluff bodies and surfaces

Mechanisms of deposition on solid surfaces from the flow normal to the surface are encountered in filtration and membrane operations. They also govern the collection of small droplets or particles in wet scrubbers, the deposition of super-cooled water drops on the wings of aircrafts (aircraft icing), and the build-up of deposits in cyclones and other process equipment.

An important parameter used to describe deposition on bodies from normal flows is the collection efficiency or *capture efficiency*. It is defined as the fraction of particles that are approaching the collector in the region defined by the projected area of the collector, that are ultimately deposited on the collector surface,

$$E = \frac{Mass\ of\ particles\ from\ the\ projected\ area\ deposited\ on\ the\ body}{Mass\ of\ particles\ in\ the\ projected\ area\ approaching\ the\ body} \tag{2.7}$$

The *deposition coefficient*, k_d, or *deposition velocity*, can be obtained by multiplying the capture efficiency, E, with the superficial velocity, U,

$$k_d = E \cdot U \tag{2.8}$$

The deposition rate, r_d, is then obtained by multiplying the deposition coefficient, surface area, A, and concentration, c_b,

$$r_d = k_d \cdot c_b \cdot A \tag{2.9}$$

As described by Hinds [20] and Friedlander [21], the main collection mechanisms that govern deposition from a normal flow are: interception, inertial impaction, diffusion, gravitational settling, electrostatic attraction and thermal forces. However, all these mechanisms rarely occur simultaneously – usually one or two mechanisms dominate the deposition process.

Collection by *interception* occurs when a particle follows a gas streamline that is within one particle radius from the body. A particle will be captured because of its size; the larger the particle, the greater the possibility for interception. This is the only mechanism that is not a result of a particle departing from its original gas streamline. The main parameter that controls interception is the ratio of the particle, D_p, and body diameters, D_c, i.e., $R_I = D_p / D_c$.

Inertial impaction occurs when particles, because of their inertia, are unable to adjust to the change in direction of the flow in the vicinity of the body. Their path starts to deviate from the fluid streamlines, and if the inertia is sufficiently large, particles can reach the surface. The main parameter that controls inertial impaction is the Stokes number, defined as a ratio of particle stopping distance, S_p, and the diameter of the body,

$$St = \frac{S_p}{D_c} = \frac{t_p U}{D_c} \tag{2.10}$$

In the *diffusion regime*, Brownian motion of small particles causes deviation of particles from the fluid streamlines, and particles can reach the surface. Diffusion depends on the flow characteristics, and therefore the Brownian diffusion coefficient (Eq. (2.1)) should be used in empirical correlations for mass transfer to obtain the deposition coefficient.

Gravitational settling can increase the capture efficiency if the flow is in the direction of gravity, or decrease the capture efficiency if it is in the opposite direction. It is important for larger particles only ($t_p^+ > 1$).

Electrostatic deposition can be important, but it requires knowing the charge of the collector and the particles. *Thermal forces,* which include *thermophoresis* (migration of particles down a temperature gradient close to the surface) and the *thermoelectric effect* (heat flux induced thermoelectric voltage in the adjacent coolant stream), can be important, but only when temperature gradients exist.

For deposition onto body and surface collectors normal to the flow, we can distinguish between the deposition on the upstream (front) side, and deposition on the downstream (back) side, since each side is characterized by a different flow field.

2.2.1. Upstream (front) side

In the literature, it is mainly the inertial impaction mechanism on the upstream (front) surface of single elements that has been studied, both theoretically and experimentally. Early work on the theory of inertial impaction was done by Albrecht [22], Sell [23], Langmuir and Blodgett [24] and Landhal and Herrmann [25]. Their results differed to some degree, depending on the flow approximation, position where the particles were injected, and number of particles, but the results of Langmuir and Blodget were mainly consistent with the results obtained later on. Early experimental measurements by Landhal and Herman [25] and Sell [23], due to the complexity of the phenomena involved, were not successful in separating inertial effects from the diffusion and interception effects. However, results on inertial impaction obtained by Ranz and Wong [26], Wong et al. [27] and May and Clifford [28], could be considered correct. Table 2.1 summarizes the main theoretical and experimental results on inertial impaction.

It is worth noting that, according to the theoretical predictions from the literature [30], disks showed the highest capture efficiencies among all simple geometries (ribbon, sphere, cylinder). Also, the ideal flow approximation seemed to be a satisfactory description of the flow in front of the body, in all cases. In the body of experimental data, there are discrepancies among the results, depending on whether particles or droplets are used, and how the flow was oriented. In order to explain experimental capture efficiencies lower than theoretical predictions, Wong et al. [27] suggested that viscous forces should decrease capture efficiencies. Golovin and Putnam [30] suggested the same, but for targets of the order of few centimetres in size (1–2 inches), viscosity effects

should be negligible if Re_{target}>100. The results of May and Clifford are just slightly below the potential flow predictions for horizontal flow. This is probably because the flow was oriented upward, with gravity acting in the opposite direction to the flow, suggesting that gravity could be responsible (remark of Vincent and Humphries [19]), and not the viscous forces.

Experimental results from the literature, along with a theoretical prediction of inertial impaction on disks, are given in Figure 2.2. Calculations and experimental data are given for horizontal flow (except May and Clifford [28], upward flow). It can be seen that the capture efficiencies can be presented as a unique function of the Stokes number. As the Stokes number is increased, particles possess more inertia, and are unable to closely follow the fluid streamlines that go around the body. As a result, particles impact the surface and deposit.

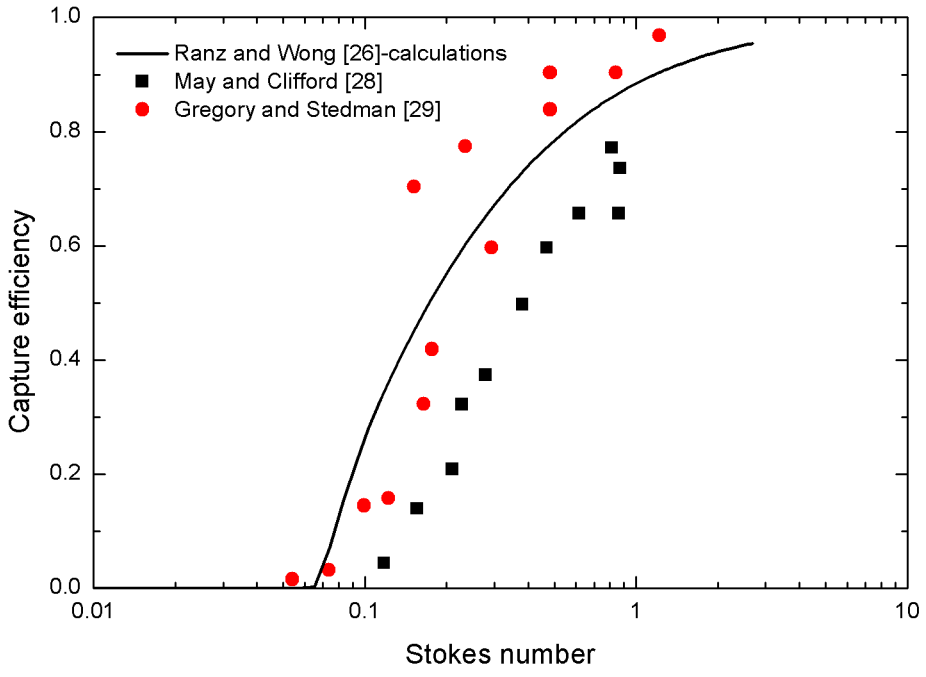

Figure 2.2 Experimental and theoretical data on inertial deposition onto front surfaces of disks

Table 2.1 Summary of experimental data and simple theoretical treatments of inertial impaction on the front side of bluff bodies

Authors	Theory		Experiments		
	Shape	**Simulation**	**Shape**	**Materials (solid particles/droplets)**	**Measurements**
Langmuir and Blodgett [24]	Cylinder, Sphere, Ribbon	Potential flow, no gravity, non-Stokesian drag force	–	–	–
Ranz and Wong [26]	*Disk*, Ribbon	Potential flow, no gravity, Stokes drag force	Cylinder, Sphere	No indications on the flow orientation. Nearly uniform 0.3–1.4 micron droplets of concentrated sulphuric acid (aerosol condensation generator). Collectors: 3-mil platinum wires and 0.9 mm platinum sphere	Droplet size not measured, but controlled by changing operating conditions of the aerosol generator. Weight of deposits measured after the experiment.
Gregory and Stedman [29]	–	–	*Disks*, Cylinders, Stripes	Horizontal flow. Lycopodium spores, about 28 micron diameter. Velocity: 0.5–9.5 m/s	Direct counting of deposited spores under the microscope
Wong et al. [27]	Cylinders	Potential flow, no gravity, Stokes drag force	Cylinders	No indications on the flow orientation. 0.6–1.4 micron uniform droplets, concentrated sulphuric acid (homogeneous aerosol generator). Collectors: 29–106 micron platinum wires. Velocity: 4–50 m/s, Reynolds number: 13–330	Droplet size not measured, but controlled by changing aerosol generator operating conditions. Weight measured after the experiment.
Golovin and Putnam [30], review article	Cylinders, Spheres, Ribbon, Airfoils at different angles	Potential flow theories, no gravity, Stokes drag force	Cylinders	Reviewed experimental results for cylinders: Gregory and Stedman (1953), Ranz and Wong (1952), Ranz, Wong and Johnstone (1954), Amelin and Belyakov (1956)	-
May and Clifford [28]	–	–	*Disks*, Cylinders, Spheres, Ribbons	Upward flow. Uniform dibutyl phthalate droplets 20, 30, 40 microns in diameter (aerosol spinning top generator). Velocity: 2.2–6.2 m/s in the 20×20 cm wind tunnel. Targets: 0.1–2.9 cm (disks: 0.154, 0.480, 0.995, 1.431, 2.875cm). Reynolds: 165–8500.	Droplets size measured by magnesium oxide method. No indications on measurements of the weight of deposits.
Noll and Pilat [31]	Ribbon, Half-body	Potential flow, no gravity, non-Stokesian drag force	Ribbon, Half-body	Flow orientation is not evident. Size distribution of the atmospheric aerosol, with particles larger than 1 micron.	Aerosol size distribution measured in the Atmospheric giant particle inertial impactor.
Vincent and Humphries [19]		–	*Disks*	Horizontal flow. Size distribution of dusts. 5 cm diameter disk.	10 times lower efficiencies. Close to the rim there was no dust deposits (bounced off or re-entrained).

Although it does affect capture efficiencies, gravity was often not considered important, and in most cases it was not explicitly stated if the experiments were performed with horizontal, upward or downward flow. From the description of the experimental procedures and the pictures of the experimental setup, it seems that only the experiments of May and Clifford were performed in upward flow, and all others in horizontal flow. In their calculations, Tsai and Liang [32] studied inertial effects along with gravity from the axisymmetric stagnation point flow approximation, but the presented results were for the gravity in the flow direction only. Also, experimental results were available only for small blockage ratio ($Br \approx 0.05$, May and Clifford [28]), where the effect of column walls or other neighbour elements, have a negligible effect on the flow field and deposition.

Experimental investigation of deposition due to convective diffusion and inertial mechanisms from turbulent flow onto normal surfaces has not been reported in the past, to the best of our knowledge. These deposition mechanisms lead to small amounts of deposits, compared to other mechanisms encountered in normal flow (inertia, gravity or interception). Successful separation of these mechanisms would require working with small droplets (a few microns), flowing over targets in the range of few centimeters. Removal of small droplets was of primary interest in fiber filter technology and was therefore mainly studied for the flow over small fibers (<100 microns), where inertia and interception are the dominating mechanisms.

2.2.2. Downstream (back) side

Deposition on the downstream (back) side of bluff bodies did not attract much attention of researchers in the past; probably because in the majority of applications, the upstream side collected significantly more deposits. Also, the imprecisely defined turbulent wake behind the disk did not allow theoretical treatment, and deposition could be investigated only experimentally.

Experimental results on the downstream surface were reported by Amelin and Beliyakov [33], who investigated capture efficiencies of the front and back sides of cylinders. As explained by Golovin and Putnam [30], their results showed a linear increase with increased Stokes number (i.e., due to increased velocity). However, the results could not be considered reliable, since their lowest capture efficiencies were of

order 10^{-6}, while just due to the interception, capture efficiencies should be at least 10^{-4}. Yeomans et al. [34] investigated deposition of DDT solutions on the front and back surfaces of glass discs and leaves in still and moving air. They found that for small particles, deposition on the downstream side exceeded deposition on the upstream side. As the Stokes number was increased (by increasing the drop size), capture efficiencies first increased. At about a Stokes number of 0.06 (calculated from VMD=15 micron, at U=3.6 m/s), the capture efficiencies started decreasing steadily toward zero. At this value, the amount of deposits on the upstream and downstream sides was similar.

Goldshmid and Calvert [35], measured deposition of small particles (0.8–2.8 microns) on oscillating drops and observed that for particles below 1 micron in size, capture efficiencies suddenly increased. They tried to explain this by claiming that the deposition takes place in the vortex behind the disk. They employed a simple model based on inertial deposition from the vortex (centrifugal force of particles), which was able to qualitatively explain the results.

Vincent and Humphries [19] measured capture efficiencies of dusts onto the front and back surfaces of disks. For the back side, their results showed a decreasing trend with velocity and increasing trend with particle size. The results also showed that the back side capture efficiencies could not be represented solely as a function of the Stokes number. In trying to explain the mechanisms of deposition, they did not consider inertial impaction or gravity, but mentioned turbulent diffusion, Brownian diffusion and electrostatic forces.

Again, in none of the works mentioned above was gravity considered important enough to be mentioned how experiments were performed, and whether or not it could have had an effect on deposition. Table 2.2 summarizes the main results on downstream deposition.

Table 2.2 Summary of experimental investigations for the downstream (back) side of bluff bodies

Authors	Shapes	Materials	Measurements
Amelin and Beliyakov [33]	Cylinders	n/a	n/a
Yeomans et al. [34]	Glass, wire cloth, filter paper and leaf *disks* (4.1–15 cm in diameter)	Horizontal flow in the 18m long wind tunnel. Droplets of DDT in petroleum (VMD: 8.4 – 33.0 microns) via La Mer-Sinclair homogeneous aerosol generator. Velocities: 3.2 to 25.6 km/h.	Weight of DDT deposits at the end of experiment, counting dead mosquitoes, measuring median diameter
Goldshmid and Calvert [35]	Oscillating drops	La Mer-Sinclair homogeneous aerosol generator. Drops of formamide, hexadecane, water and glycerol. Polystyrene particles and sulfur droplets, 0.8–2.8 microns in size.	Counting of polystyrene particles and weighing of sulfur deposits
Vincent and Humphries [19]	Metallic *disks*	Horizontal flow. Graded dusts of brown aloxite, size distribution with median diameter 3.0, 6.5, 13.0 and 17.0 microns. Disks 2.0, 2.8, 5.0 and 10.0 cm diameter.	n/a

In summary, the inertial deposition onto the upstream side of bluff bodies was investigated mainly with success: theoretically, using the inviscid flow approximation, and experimentally too, although discrepancies between the reported results exist. In all investigations, the flow orientation was not considered important and the effect of gravity was not included into the calculations (except Tsai and Liang [32]). In addition, in the investigations of particle deposition on disks, only the Stokes drag force on particles was used.

For the downstream side, there has been no computational treatment of the deposition from the wake (except by Lakghomi [36]), and the mechanisms of deposition were not understood clearly. The experimental results also showed some discrepancies; and to the best of our knowledge, no investigation on the deposition from an upward flow with droplets in the aerosol has been conducted. The following section (Section 2.3) discusses distribution of deposits along the coupon radius.

2.3. Distribution of deposits along the coupon radius

In order to predict whether some areas of packing elements in the scrubber section of the Fluid Coker would foul more rapidly and potentially become a bottleneck for the

whole scrubber, and therefore the whole reactor, the mass and size distribution of the deposits on the disk surface had to be determined.

Gregory and Stedman [29] reported higher concentrations of *Lycopodium spore* deposits at the edges of the front side of disks. This is contrary to what they observed for cylinders, in which case there were more deposits in the centre. Noll and Pilat [31] measured local capture efficiencies on the front side of ribbons and found that the pattern is similar to that on disks: more deposits were found close to the ribbon edge. These observations were explained with an inertial deposition model, which predicted more deposits toward the edge of the ribbon. Vincent and Humphries [19] noted that on the front surface of disks, deposits were concentrated close to the centre. However, their capture efficiencies were as much as 10 times below theoretical predictions. Since they worked with solid particles (aloxite dusts), they explained the discrepancies by the probable re-entrainment of dusts particles, and therefore, their results for the distribution of deposits cannot be considered reliable.

To summarize, data on the distribution of droplet deposits on the upstream sides of disks are not available in the literature. Also, distribution of deposits on the downstream side of surfaces or body collectors of any shape, to the best of our knowledge, has not been reported. This justifies our intention to determine the distribution of deposits along the radius of the disk.

2.4. Contact angle effect

The majority of the prior work on deposition was focused on particle transport to the surface, probably because it was considered more important in the fouling process. Two other factors that can affect the fouling process are droplet sticking and droplet re-entrainment. In our case, it is reasonable to assume that the re-entrainment of liquid droplets deposited on the surface of the disk does not occur; these phenomena are more common for solid particles. The remaining important phenomenon is sticking, and how it can be influenced. To explain sticking, we start by explaining the wetting and contact angles.

2.4.1 Wetting and contact angles

Wetting (or *wettability*) represents the ability of a liquid to maintain contact with a solid surface, which is the result of intermolecular forces of the two phases in contact. The degree of wetting is determined by the equilibrium of adhesive forces between the solid and the liquid, and cohesive forces within the liquid. If the adhesive forces are stronger, the degree of wetting will be higher.

Contact angle represents a quantitative measure of wettability, and the relative strength of adhesive and cohesive forces. It is the angle, θ, between the tangent lines of the liquid-vapour and the solid-vapour interfaces, as presented in Fig. 2.3.

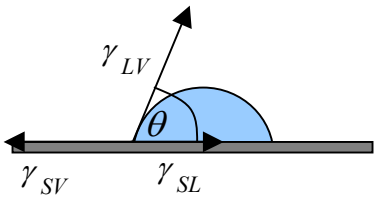

Figure 2.3 Schematic representation of the surface tension forces acting on a droplet deposited on the surface

From a force balance along the three-phase interface, the following relation can be devised (Young's equation): $\gamma_{SV} - \gamma_{SL} = \gamma_{LV} \cos(\theta)$, where γ_{SV}, γ_{SL}, γ_{LV} are the surface tensions on the solid-vapour, solid-liquid and liquid-vapour interface respectively. This equation is often approximated as $\gamma_S - \gamma_{SL} = \gamma_L \cos(\theta)$, where γ_S and γ_L are the surface tensions of the solid and liquid.

The *surface tension* of liquid represents the energy required for a unit increase in area of the liquid-gas interface. Surface tensions of solids have the same meaning. Usually, they are referred to as *surface energy*. Exact measurements are difficult, and according to Marere and Douillard [37], currently assumed values for surface energies of solids are 10–72 mJ/m^2 for low energy solids (e.g. polymers, carbons, and sulfurs), 72–200 mJ/m^2 for middle energy surfaces (e.g. clays and clay minerals, silicas, quartz) and 200–2000 mJ/m^2 for high energy solids (e.g. metals) [37]. Surface tensions of liquids

at 20°C vary from 20–75 mJ/m^2; the exception is mercury with surface tension of 425 mJ/m^2. Table 2.3 summarizes possible combinations of liquid-solids interactions and the relation with contact angles and wettability.

Table 2.3 Degree of wetting explained in terms of solid-liquid and liquid-liquid interaction

Contact angle	Degree of wetting	Strength of	
		S/L interactions	L/L interactions
$\theta = 0^\circ$	Perfect wetting	Strong	Weak
$0^\circ < \theta \leq 90^\circ$	High wettability	Strong Weak	Strong Weak
$90^\circ < \theta < 180^\circ$	Low wettability	Weak	Strong
$\theta = 180^\circ$	Perfect non-wetting	Weak	Strong

From Table 2.3, it can be seen that low wettability can be achieved with strong liquid-liquid interactions and weak solid-liquid interactions. Strong L/L interactions are characterized by high surface tension of the liquid, and weak solid-liquid interactions are usually result of low surface energies of solids (the majority of high surface energy solids wet all liquids, i.e. metals, while low surface energy solids give low wetting, i.e. Teflon). The following table shows contact angles of water at 20°C (γ=73 mJ/m^2), with different surface energy solids [38].

Table 2.4 Contact angles of water at 20°C with solids of different surface energies [38]

Material	Surface energy (mJ/m^2)	Contact angle (°)
Clean glass	73	0
Ordinary glass	70	20
Platinum	62	40
Anodized aluminium	50	60
Polymethyl-methacrylate	41	74
Nylon	38	79
Polyethylene	33	96
Polypropylene	26	108
Paraffin	19	110
Teflon	18	112

From this table, we can see that as the surface energy is decreased, contact angles are increased. The role of contact angles in droplet sticking or rebounding is explained in the next section.

2.4.2. Impact of droplets on the solid surface (sticking vs. rebounding)

The phenomena governing liquid impacts on solid surfaces are quite complex, and more complicated than those encountered on wetted surfaces. The reason for the additional complexity is the influence of surface texture, i.e. wettability and surface roughness (Yarin [39]). The main types of behaviour when a droplet impacts a dry solid surface (Table 2.5) can be described as follows [39, 40].

a. Deposition. The droplet spreads upon impact and stays deposited on the surface. This mostly occurs with hydrophilic (and oleophilic) surfaces ($\theta < 90°$), but it can also happen with hydrophobic (and oleophobic) surfaces ($\theta > 90°$). For hydrophobic surfaces, it occurs when force that is acting to remove the droplet from the surface is sufficiently small, i.e. droplet deposition velocity is so small that there is no bouncing and the droplet stays on the surface; or, the gravity force on the droplet resting on a slightly inclined hydrophobic surface is not sufficient to cause sliding.

b. Splashing (*prompt splash* or *corona splash*). An increased impact velocity on a hydrophilic rough surface causes tiny droplets to detach from the edge of the lamella (*prompt splash*), and if the surface tension of the liquid is reduced, lamella are able to detach from the wall (*corona splash*). If the impact velocity is high enough, splashing or breakup can also occur on hydrophobic and superhydrophobic surfaces ($\theta > 150°$).

c. Rebounding. Rebounding happens most often on hydrophobic surfaces, although according to the simulations of Khatavkar [41], partial rebounding can occur on hydrophilic surfaces also. Rebounding follows retraction of a droplet from the elongated state, where its initial kinetic energy is transformed into the potential energy of surface tension (and partly dissipated inside the droplet via viscous dissipation). If, in retracting, the droplet-surface interactions are strong (hydrophilic surface or hydrophobic surface), and viscous dissipation is present, only partial rebounding can occur. However, if the surface is superhydrophobic, droplet-surface interactions are negligible, and the droplet can fully rebound. This can happen only if viscous dissipation is not significant: e.g. it is unlikely that a drop of honey would rebound from any surface. In addition, advancing and receding contact angles (θ_{adv} and θ_{rec}) should be similar, in order to avoid contact angle hysteresis as a significant source of energy dissipation.

Table 2.5 Possible outcomes of droplet impact on a solid surface

Deposition (drop oscillates a little)	Prompt splash	Corona splash	Partial rebounding	Complete rebounding
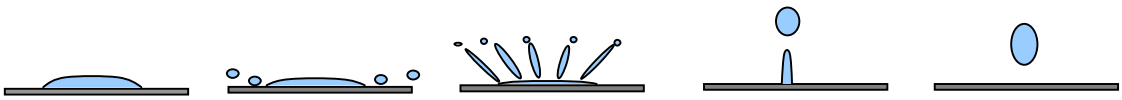				

To reduce fouling, we are interested in *partial* or *complete rebounding*. From experimental observations, it is known that complete rebounding can occur only on high contact angle surfaces (θ>150°), classified as superhydrophobic surfaces [42, 43, 44]. In nature, examples are the surfaces of the lotus leaf (*Nelumbo Nucifera*), or bird feathers. In addition to having a hydrophobic waxy layer, their surface is enhanced with two levels of roughness on the microscale. The first level consists of 10–20 micron size bumps that do not allow large droplets to penetrate between them. The second level of roughness is made of below micron-size hairs, densely packed all over the surface. Droplets sitting on such surfaces are found in the so-called Cassie state: pockets of air remain below the droplets, and apparent contact angles between the liquid and the surface are usually greater then 150°.

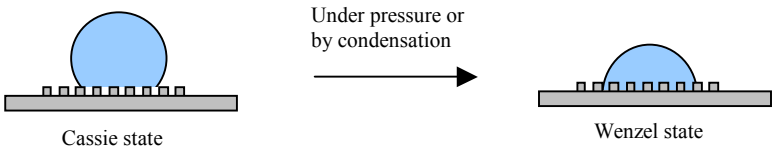

Figure 2.4 Droplet on a surface in the Cassie (metastable) state, showing superhydrophobic properties, and in the Wenzel (stable) state, wetting the surface

However, if exposed to increased pressures (e.g. by submerging at certain depths under the water), these surfaces could lose their properties and undergo transition into the Wenzel state, where droplets actually wet the surface. Indeed, recent experiments showed that the surface of the lotus leaf is covered with a hydrophilic (not hydrophobic) waxy layer (θ=74°), and that it loses its superhydrophobic properties if under pressure, or if condensation occurs [45, 46]. In addition, pressure from the droplet impact can cause penetration of water into asperities and wetting of the surface (Wenzel state).

A good review of possible outcomes of drop impact on superhydrophobic surfaces, depending on the impact velocity and Wenzel roughness is given by Rioboo et al. [47]. Their experiments also showed that droplets below 0.1 mm, in the range of impact velocities from 0.1 to 10 m/s, would rebound or stay deposited on the surface. If droplets stayed deposited on the surface, they were in the Cassie state and could be easily removed. Richard and Quere [44] investigated the bouncing of water drops from a superhydrophobic surface with a contact angle of 170°, and noted perfect droplet bouncing with the coefficient of restitution close to 0.9. Bouncing and splashing of droplets on 150° surface was investigated also by Durickovic and Varland [44]. Wang et al. [48] investigated rebounding of water drops from carbon nanotube arrays and observed that for contact angles of 163°, the droplets would bounce off several times, while for contact angles of 140°, they remained pinned to the surface.

Bergeron [69], in his popular article on deposition of droplets on the leaves of plants in agricultural applications, explained that sticking or rebounding is governed by inertial, viscous and capillary forces of the drop upon the impact. One way to increase deposition is to reduce the surface tension of the liquid or increase its viscosity; for reducing deposition, the opposite holds. Therefore, in order to promote droplet bouncing, one could:

- Increase contact angle, by using low surface energy solids (e.g. Teflon), to achieve partial rebounding.
- Increase contact angle, by using superhydrophobic surfaces ($\theta > 150°$), to achieve complete rebounding.

In addition, one could promote rebounding by:

- Decreasing the viscosity of the liquid, so that the droplet upon impact does not lose energy via viscous dissipation, and has more energy to bounce off.
- Increasing the surface tension of the liquid, in order to increase the contact angle and decrease the wettability.

Since the superolophobic surfaces with high contact angles look as the most promising for our application, they are discussed in more details in the next section (Section 2.3.4).

2.4.3. Superoleophobicity

Recently, a number of authors have reported that they have synthesised surfaces which manifest superhydrophobicity and superoleophobicity at the same time. The first to report super-oil repellent surfaces were Tsujii et al. [49], who coated fractal structures on an oxidized aluminum plate surface with the trifluoromethyl groups of fluorinated monoalkylphosphates. They obtained high contact angles; for rapeseed oil 150°, and for octane 120°. Tuteja et al. [50,51] described designing parameters for such surfaces, and explained that for high contact angles of low surface tension oils, such as decane (23.8 mN/m) and octane (21.6 mN/m), a surface energy of a smooth solid of the order of 5 mN/m was needed. They synthesised a new class of hydrophobic fluoroPOSS molecules (Fluorinated Polyhedral Oligomeric Silsesquioxanes), to cover the roughened surface. Advancing and receding contact angles were 163° and 145° respectively. Wu et al. [52] treated alumina nanowire forests with perfluorocompounds and obtained contact angles higher than 150° for different oils (155.6° for crude oil, 150.4° for silicone oil).

High contact angles of oils make them potentially useful for application in causing the rebounding of oil droplets in the scrubber of the coker reactor. However, since all these surfaces are treated with organic compounds (fluoro-groups, silanes) with relatively low melting points, their application at high temperatures above 300°C is questionable. Fractal surfaces of Teflon (melting point 327°C) may provide better performance. Recently, Cao et al. [70] reported superhydrophobic surfaces (water contact angle 159 ± 2°) produced by packing flowerlike hematite particles which are intrinsically hydrophilic. The largest asperities on the surface seemed to be in the order of 1 micron, and such surfaces did not lose their properties after heating in air at 800°C for 10 hours (θ=158 ± 2°). However, they did not report tests with oils.

In the case of the scrubber section of the coker reactor, it seems that only complete rebounding could be considered as an option. Partial rebounding would leave some amount of deposits on the surface, which would eventually form a monolayer of coke deposits and the repellent surface properties would diminish. However, superhydrophobic surfaces have also ‘self-cleaning’ properties. Lotus leaves, feathers of birds, etc. have the property of using the water to collect all the dirt (i.e. small particles)

from their surface, while rolling down the surface. In that sense, even partial rebounding of bitumen droplets from superhydrophobic surfaces could be satisfactory. If the wash-oil that is poured from the top doesn't wet the surface, it would roll off the surface, collecting deposited bitumen droplets. Still, many practical questions remain,

- How long could superoleophobic surface be maintained clean, i.e. whether small bitumen droplets would deposit inside the microstructures so that they could not be reached and picked up by the liquid flowing down? How small should asperities on the surface be, to prevent that from happening?
- How would superhydrophobic surfaces behave at high temperatures, would they be stable, without sintering?
- Would the metastable Cassie state be diminished if the droplet impacting the surface possesses sufficient pressure to penetrate inside the pores? Is the wash-oil sprayed from the top more likely to do so?
- Does the condensation of vapours in the scrubber section occur? If so, surfaces would most probably lose the feature of superoleophobicity.

To summarize, for complete rebounding, superhydrophobic and superolephobic surfaces, with contact angles higher than 150° are required. To repel oil droplets, in addition to the fractal structure of surface roughness, low surface energy materials are needed. Since such surfaces are not commercially available yet, we decided to test surfaces with contact angles in the range that could be obtained (20–94°) and see if partial rebounding [41] could reduce deposition rates. Goldshmid and Calvert [35], who investigated the collection of polystyrene and sulphur particles from aerosols onto supported liquid drops (water, glycerol, formamide, phenol), showed that with an increased contact angle in the range from 0° to 87°, there is "definite effect of interfacial tension on the collection efficiency". These results also justify our attempts to investigate the contact angle effect in a similar range.